Bulletin of the Seismological Society of America, Vol. 92, No. 4, pp. 1433–1442, May 2002

The 1999 (M_w 7.1) Hector Mine, California, Earthquake: Near-Field Postseismic Deformation from ERS Interferometry

by Allison Jacobs, David Sandwell, Yuri Fialko, and Lydie Sichoix

Abstract Interferometric synthetic aperture radar (InSAR) data over the area of the Hector Mine earthquake (M_w 7.1, 16 October 1999) reveal postseismic deformation of several centimeters over a spatial scale of 0.5 to 50 km. We analyzed seven SAR acquisitions to form interferograms over four time periods after the event. The main deformations seen in the line-of-sight (LOS) displacement maps are a region of subsidence (60 mm LOS increase) on the northern end of the fault, a region of uplift (45 mm LOS decrease) located to the northeast of the primary fault bend, and a linear trough running along the main rupture having a depth of up to 15 mm and a width of about 2 km. We correlate these features with a double left-bending, right-lateral, strike-slip fault that exhibits contraction on the restraining side and extension along the releasing side of the fault bends. The temporal variations in the near-fault postseismic deformation are consistent with a characteristic time scale of 135 + 42 or − 25 days, which is similar to the relaxation times following the 1992 Landers earthquake. High gradients in the LOS displacements occur on the fault trace, consistent with afterslip on the earthquake rupture. We derive an afterslip model by inverting the LOS data from both the ascending and descending orbits. Our model indicates that much of the afterslip occurs at depths of less than 3 to 4 km.

Introduction

The Hector Mine earthquake (M_w 7.1, 16 October 1999) ruptured the surface along the Lavic Lake fault, the Bullion fault, and sections of several other faults within the eastern California shear zone (ECSZ) (Fig. 1) (Dibblee, 1966; USGS *et al.*, 2000; Treiman *et al.*, 2002). The ECSZ contains a series of northwest-trending faults that collectively take up a substantial amount of the motion between the Pacific and North American plates (Dokka and Travis, 1990). InSAR observations in the area of the nearby 1992 Landers earthquake reveal transient deformation localized near the earthquake rupture, highlighting the importance of monitoring the near-field postseismic deformation (Massonnet *et al.*, 1993, 1994; Zebker *et al.*, 1994; Peltzer *et al.*, 1996). To obtain adequate InSAR coverage of the crustal deformation following the Hector Mine earthquake, we asked the European Space Agency to continue acquiring SAR data in the region. To date, four high-quality postseismic interferograms can be constructed, and we expect more will become available as additional ERS-2 SAR data are collected in 2002.

Our analysis of the Hector Mine earthquake focused on the near-field (<50 km from the rupture) postseismic deformation, using SAR data collected by the European Space Agency satellite ERS-2. Although a number of GPS measurements collected after the earthquake may provide constraints on the larger-scale deformation (>50 km) (Agnew *et al.*, 2002; Owen *et al.*, 2002), they lack the spatial resolution to characterize the details of postseismic deformation within 10 km of the main rupture. The large-scale postseismic deformation has also been analyzed using two of the four interferograms presented here (Pollitz *et al.*, 2001). These larger-scale studies have been interpreted in terms of viscoelastic deformation of the lower crust–upper mantle; however, we believe this interpretation is premature, because the observed LOS displacements are small (on the order of a few centimeters) and are not correlated between different interferograms, suggesting that they might be atmospheric artifacts.

Here we examine postseismic deformation over four time periods: 4 to 249 days, 39 to 144 days, 74 to 319 days, and 39 to 354 days after the earthquake (Fig. 2). The four interferograms, derived from seven independent SAR acquisitions, all show consistent patterns. This enables us to perform a quantitative analysis of the postseismic decay time. There were only two large aftershocks (>M_w 5.0) in this combined time period, and these occurred well north of the main rupture, so the deformation we have observed is likely aseismic.

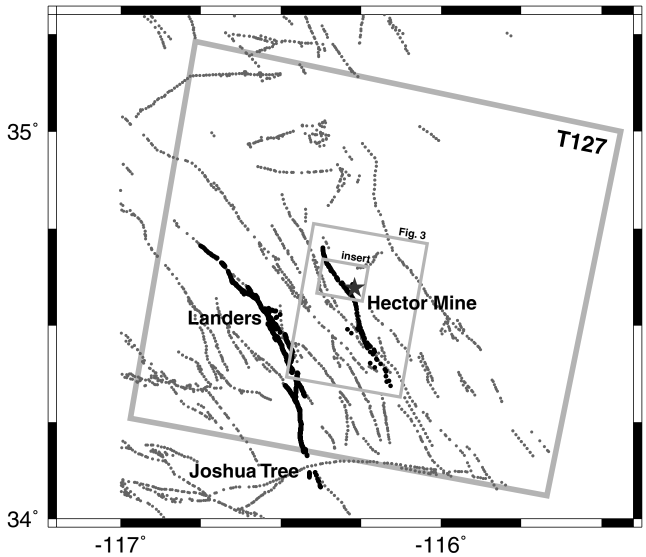

Figure 1. Location map of the 1999 Hector Mine earthquake within the eastern California shear zone and in relation to the Landers and Joshua Tree earthquakes. Star indicates the epicenter of the Hector Mine main shock. The largest gray box indicates the European Space Agency's ERS-2 satellite track 127, which images the region of interest. Two smaller gray boxes show area of detailed analysis (Fig. 3).

InSAR Processing

We use repeat-pass interferometry (Zebker *at al.*, 1994; Massonnet and Feigl, 1998; Price, 1999; Rosen *et al.*, 2000) to create LOS displacement maps of an area about 110 km by 110 km surrounding the rupture (Fig. 1). The *X*-band receiving station at Scripps Institution of Oceanography was initially used to acquire these data, so they could be processed in near real-time, although later the data were obtained from ESA through its distributors, SpotImage and Eurimage. Figure 2 gives the perpendicular baselines of the relevant data from the descending track across the Hector Mine earthquake area (ERS track 127), using precise orbital information from Delft Technical University (Scharroo and Visser, 1998). The topographic phase was removed during each interferogram formation to isolate the deformation phase. The USGS 90-m topography was used to help unwrap the phase of a long-baseline (195 m) topographic pair. The residual phase of each interferogram was unwrapped (Goldstein *et al.*, 1988) and transformed into LOS displacement. A best-fitting plane was removed from each displacement map to account for possible errors due to imprecise orbits. Such detrending does not introduce any spurious signal to the LOS data on length scales less than ~50 km. We refer to these maps as postseismic pairs 1, 2, 3, and 4, as shown in the timeline (Fig. 2).

The ERS satellites measure LOS displacement at an angle of about 23° from vertical, such that the LOS displacements are more sensitive to vertical rather than horizontal motion. The steep look angle of the ERS satellites impedes precise estimates of pure strike-slip fault offsets (Massonnet and Feigl, 1998). Furthermore, the faults in the eastern California shear zone lie at high angles to the look direction of the radar from the descending orbit and nearly perpendicular to the look direction from the ascending orbit. Radar data from the ascending orbits is quite limited, so determination of vector offsets in postseismic deformation is a considerable challenge.

Postseismic Deformation

The LOS deformation maps for each of the four postseismic intervals show long-wavelength deformation patterns that are highly variable and dependent on the plane removed from each map. Although our postseismic interferogram 1 (full interferogram not presented here) shows general agreement with the corresponding interferogram published by Pollitz *et al.* (2001), we do not yet believe that the large-scale pattern is related to crustal deformation, because several other interferograms show different large-scale patterns. In contrast, at the smaller scale (<50 km), each inter-

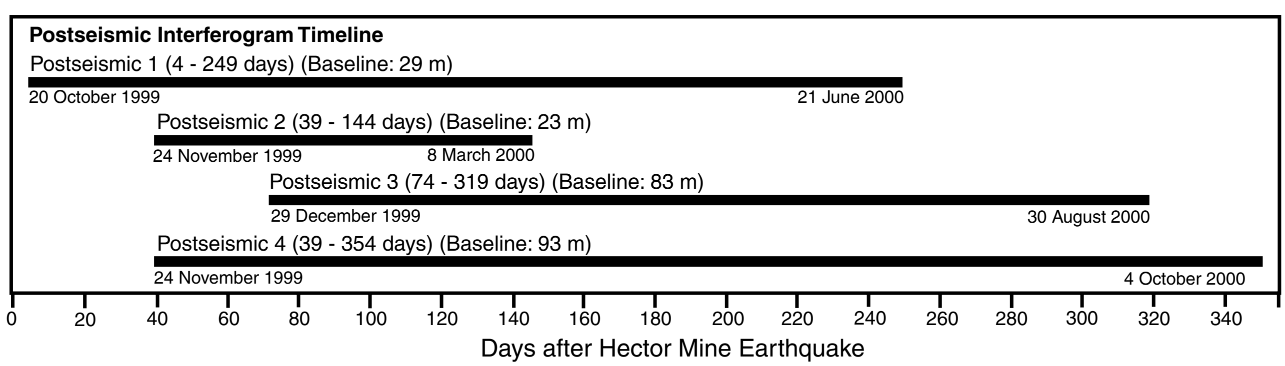

Figure 2. Timeline of postseismic interferograms showing the time span of each postseismic pair relative to days after the Hector Mine earthquake. Also presented are the dates of each image within an interferometric pair, along with the perpendicular baseline for each pair.

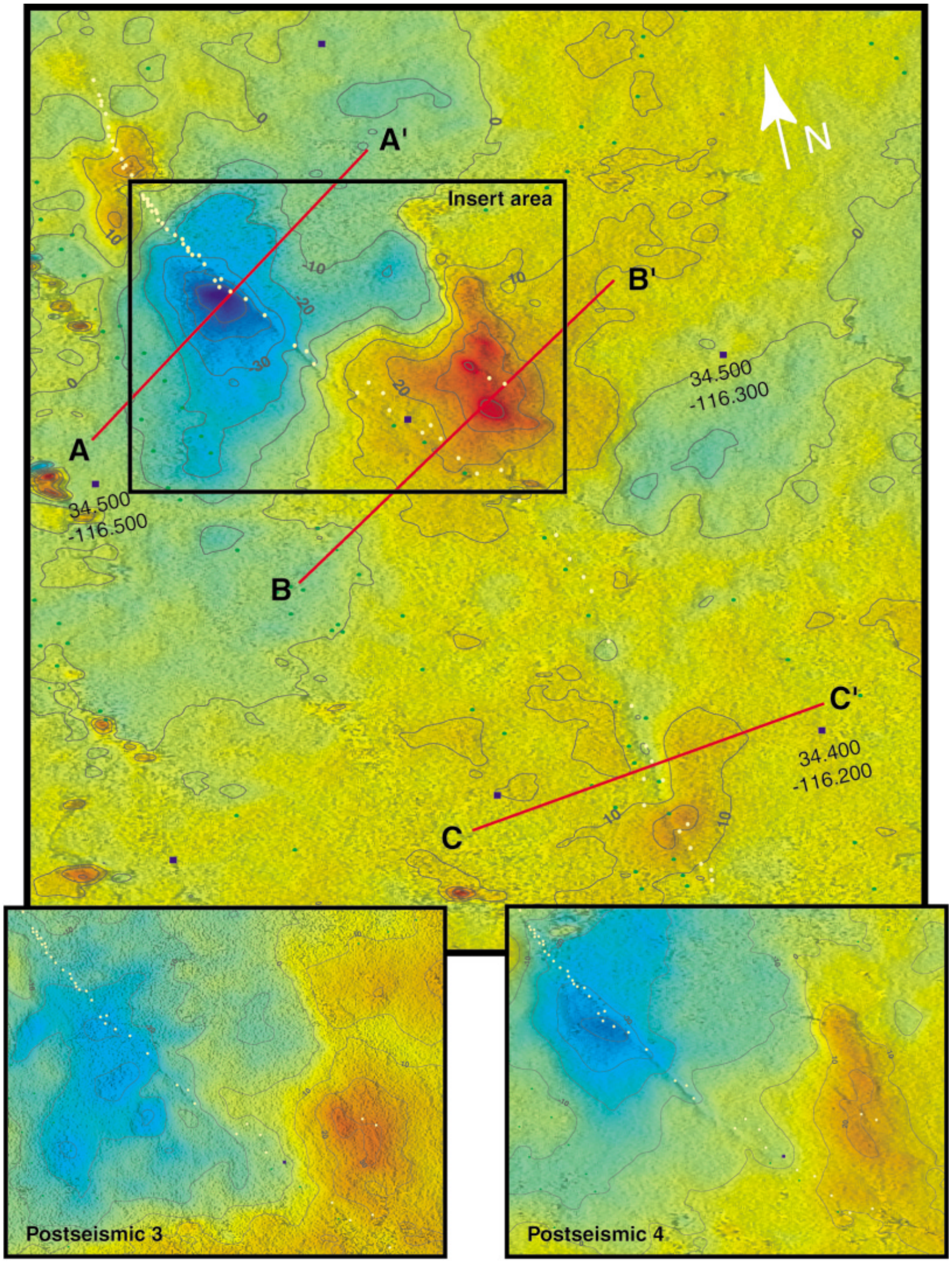

Figure 3. Postseismic 1 LOS displacement (large image) between day 4 and 249 after the Hector Mine earthquake (10-mm contour intervals). Color scale varies from dark blue, representing the greatest away-from-satellite displacement (max. ~65 mm), to red, representing the maximum toward-satellite displacement (max. ~40 mm). Red lines correspond to profiles drawn across the fault (Fig. 4). Yellow dots correspond to the USGS-mapped Hector Mine fault rupture, while the green dots represent other mapped faults in the surrounding area. Blue dots are plotted at a tenth of degree latitude and longitude for location reference. The three smaller boxes, postseismic 1, postseismic 3 (74–319 days), and postseismic 4 (39–354 days), highlight the region of maximum high-low displacement. The regression analysis discussed later utilizes this the data within this area. The postseismic 2 displacement map is not shown because it resembles postseismic 4 but with lower overall amplitude in accordance with its shorter time interval.

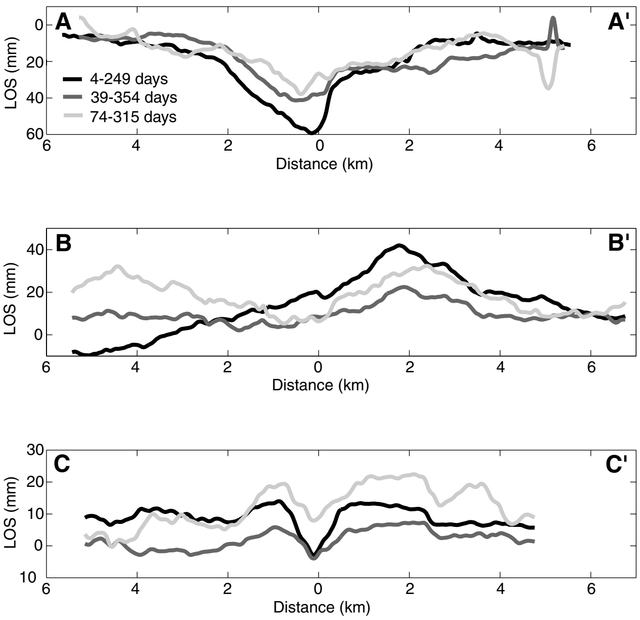

Figure 4. Profiles drawn across three areas of visible deformation on the LOS displacement maps, postseismic 1 (4–249 days), postseismic 4 (39–354 days), and postseismic 3 (74–319 days). Profile A–A′ lies across the area of subsidence seen at the northern end of the fault rupture. Profile B–B′ crosses the area of uplift located northeast of the primary fault bend. The linear trough that runs along the main rupture is exhibited in profile C–C′. (Zero distance equates to 0 km away from the fault.)

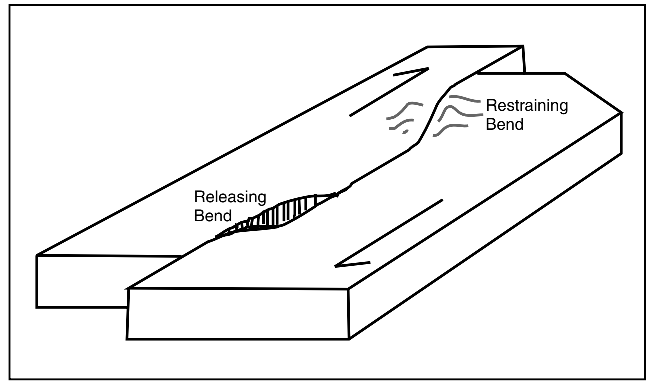

Figure 5. Schematic deformation due to a right-lateral, strike-slip fault with a double left-bend. The restraining side of the bend exhibits features associated with contraction, while the releasing bend shows extensional features (modified from Crowell, 1974).

ferogram displays a prominent near-fault signal that is well resolved by the available data (Fig. 3). Conspicuous are a region of subsidence (60 mm LOS increase) on the northern end of the fault, a region of uplift (45 mm LOS decrease) located to the northeast of the primary fault bend, and a linear trough running along the main rupture having a depth of up to 15 mm and a width of about 2 km. Profiles A–A′, B–B′, and C–C′ (Fig. 4) show the decay of the LOS displacement in the vicinity of the surface rupture. A discussion of each of the four interferograms is presented in the next section. Qualitatively, we interpret the near-fault postseismic deformation as being due to crustal relaxation following coseismic displacements on a right-lateral, strike-slip fault with a double left-bend (Fig. 5). The curvature of the fault produced a region of uplift near the restraining bend and a region of opening and subsidence near the releasing bend (Crowell, 1974; Davis and Reynolds, 1996).

Analysis of Individual Interferograms

Postseismic 1 (4–249 days; Fig. 3). All three structural features are clearly visible on this map. A broad region of LOS increase lies distinctly on the west side of the fault, with a displacement of about -60 mm (profile A–A′, Fig. 4). This might represent either true ground subsidence or right-lateral afterslip, or both. The area on the northeastern side of the rupture displays a zone of positive LOS displacements (consistent with uplift, right-lateral afterslip, or both) up to 45 mm. This LOS high occurs about 2 km east of the Lavic Lake fault and appears to decrease gradually toward the west across the fault (profile B–B′ in Fig. 4). On the east side of this high is a sharp N–S trending discontinuity, suggesting shallow slip on a N–S trending fault. The high also coincides with the approximately 1 m of east-side-up coseismic uplift (Sandwell *et al.*, 2002).

A linear trough runs along the entire rupture zone, although it is most prominent along the releasing bend of the fault (profile C–C′, Fig. 4). We believe this feature was formed by fault-zone collapse, with the greatest amplitude of subsidence in the area of extension at the releasing bend.

Postseismic 2 (39–144 days; not shown). This second LOS displacement map shows the same features as postseismic pair 1, but with lower amplitude due to its relatively short time interval (105 days). The interval time is less than one half of the time interval of the three other postseismic pairs; i.e., interferograms 1 (245 days), 3 (245 days), and 4 (315 days). The total peak-to-trough displacement seen on this map is about 50 mm, whereas postseismic map 1 shows nearly 105 mm. The greatest change between the postseismic pairs 1 and 2 is the disappearance of the along-fault trough in postseismic pair 2.

Postseismic 3 (74–319 days; Fig. 3). This interferogram starts 74 days after the earthquake and displays decreased amplitudes in all three structural features. Compared to the other three maps, this displacement map is considerably noisier, perhaps due to atmospheric effects. The broad high–low signatures still exist in the same locations and display a peak-to-trough range of about 60 mm. The trough along the rupture is apparent in this map ($\sim$10 mm), suggesting that the relaxation time is more than 74 days.

Postseismic 4 (39–354 days; Fig. 3). This displacement map has the largest time span. The LOS displacement pattern is very similar to that seen in postseismic pair 1, although the amplitudes are smaller in postseismic pair 4. This suggests that, although a large portion of postseismic deformation occurred during the 40 days after the earthquake, the process responsible for the near-fault postseismic deformation was still active beyond 1 to 2 months following the earthquake.

Near-Field Postseismic Relaxation Time

All four LOS displacement maps show the characteristic high–low pattern (Fig. 3). Assuming that this pattern is associated with a single exponential relaxation mechanism (e.g., Shen *et al.*, 1994), one can determine the relaxation time, τ, that best explains the InSAR data. The predicted LOS displacement, D, at position $\mathbf{x}$ and time t after the earthquake is given by

$$D(\mathbf{x}, t) = D_\infty(1 - \exp(-t/\tau)), \tag{1}$$

where D_∞ is the permanent postseismic deformation. The postseismic displacement map I_i measures the LOS component of deformation between the reference time, t^i_{ref}, and the repeat time, t^i_{rep}, where i is the number of a particular postseismic pair (i.e., 1 to 4). The model LOS displacement map predicted by equation (1) is

$$I_i^{\mathrm{model}} = D_\infty(\exp(-t^i_{\mathrm{ref}}/\tau) - \exp(-t^i_{\mathrm{rep}}/\tau)). \tag{2}$$

To eliminate dependence on D_∞, we take the ratio of two displacement maps corresponding to different observation times:

$$M^j_k = I_j^{\mathrm{model}}/I_k^{\mathrm{model}} = \frac{\exp(-t^j_{\mathrm{ref}}/\tau) - \exp(-t^j_{\mathrm{rep}}/\tau)}{\exp(-t^k_{\mathrm{ref}}/\tau) - \exp(-t^k_{\mathrm{rep}}/\tau)}. \tag{3}$$

From the four observed interferometric pairs, we can form six independent LOS ratios:

$$R^j_k = \frac{I_j}{I_k}. \tag{4}$$

We isolate a small section of each interferogram covering the high–low signal seen at the northern end of the fault rupture (Fig. 3, inset area). A nonbiased linear regression (i.e., functional analysis) (Mark and Church, 1977) was then used to calculate the ratio R, as well as the uncertainty σ (Fig. 6 and Table 1). This method of analysis assumes that errors exist in both the dependent and independent variables, unlike standard least-squares methods, which assume error in only one variable. The ratio of signal amplitudes about their mean value, s_{o}, is also known as the slope of the *reduced major axis* (Kermack and Haldane, 1950), and we believe it to be the best estimate of the slope. Uncertainties in the slope estimates are established using a standard least-squares technique in which the dependent variable is initially assigned all the variance and the slope, s_{xy}, of the best-fit line is calculated. Next, the uncertainty is transferred from the dependent variable to the independent variable, and the calculation is repeated. The inverted slope values for the resulting best-fit line are denoted as s_{yx}. Table 1 shows each interferometric pair along with the corresponding s_{o}, s_{xy}, and s_{yx} values, and Figure 6 exhibits all three lines superimposed upon the six regression plots from interferometric pairs.

Given these estimates of postseismic displacement ratios and their associated uncertainties, we can now calculate the best-fitting relaxation time by minimizing the weighted RMS (root mean squared) misfit, χ^2, between the observed ratio, R, and the model ratio, M.

$$\chi^2 = \frac{1}{N}\sum_N \left(\frac{M^j_k - R^j_k}{\sigma^j_k}\right)^2, \tag{5}$$

where

$$\sigma^j_k = \frac{|s_{xy} - s_{\mathrm{o}}| + |s_{yx} - s_{\mathrm{o}}|}{[2]}. \tag{6}$$

and N is the total number of independent interferometric ratios used in our analysis ($N = 6$). Since the model is nonlinear (see equation 3), we varied the relaxation time τ to find the minimum value of χ^2, as shown in Figure 7. From this analysis we obtain a relaxation time of 135 $+42$ or -25 days. The uncertainty in this estimate is taken at the points where the χ^2 curve is 10% greater than the minimum.

The relaxation time for the Hector Mine earthquake can be compared with similar estimates of time decay of the deformation following the 1992 Landers earthquake. Our inferred relaxation times are somewhat larger than the estimate of 84 $\pm$ 23 days made by Savage and Svarc (1997) and significantly larger than the 38 days calculated by Shen *et al.* (1994). An overall similarity between the characteristic relaxation times obtained from our analysis of deformation following the Hector Mine earthquake and previous results for the post-Landers deformation suggests that the same relaxation process may be responsible for the observed deformation following both events.

Possible candidates for the postseismic deformation are deep afterslip (Shen *et al.*, 1994; Bock *et al.*, 1997; Savage and Svarc, 1997), viscoelastic relaxation (Deng *et al.*, 1998; Pollitz *et al.*, 2001), and poroelastic relaxation (Peltzer *et al.*, 1996). Both deep afterslip and viscoelastic relaxation are thought to occur in the lower crust (~15–30 km depth); poroelastic relaxation is believed to take place in the upper crust (0–15 km depth).

Afterslip is presumed to occur on the lower crustal extension of the seismogenic fault, and the viscoelastic relaxation is likely to involve the bulk of the lower crust. Although the two lower-crust deformation mechanisms give rise to very similar horizontal displacements at the Earth's surface, the predicted vertical displacements are substantially different. This potentially allows one to distinguish the

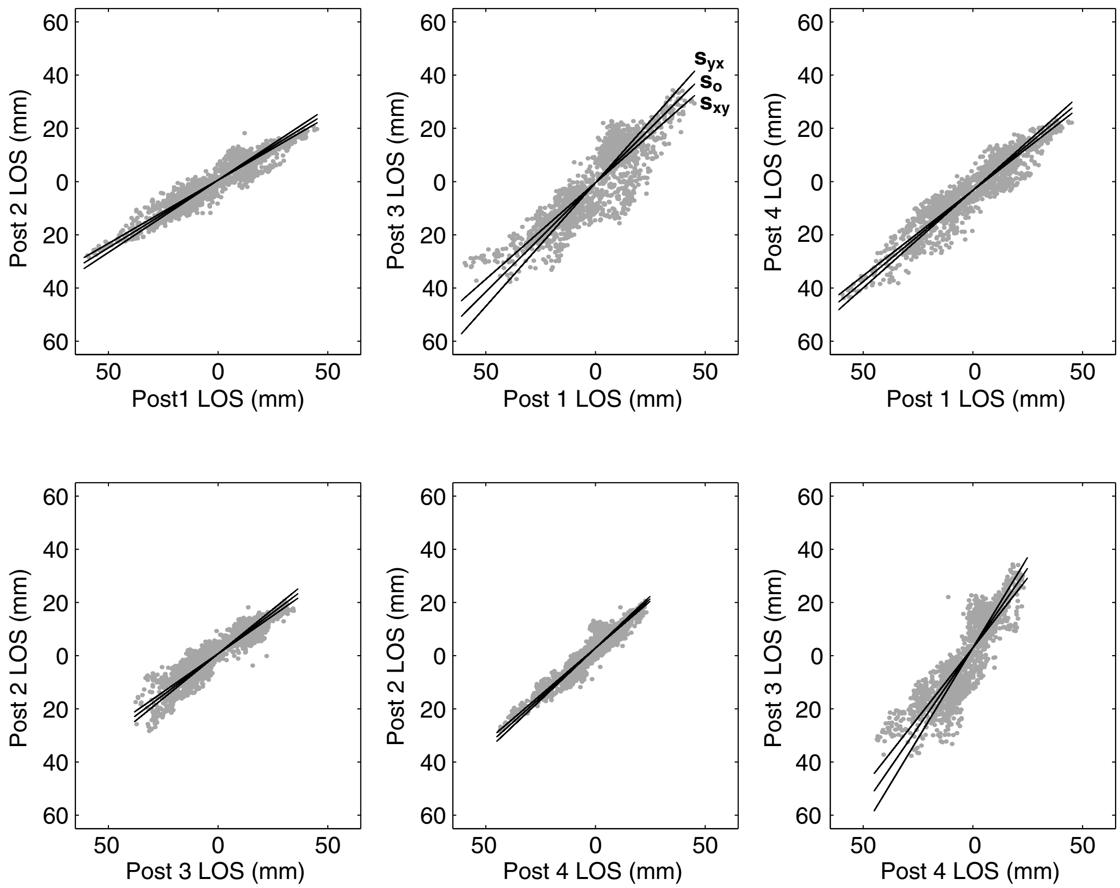

Figure 6. Plot of the six pairs of interferograms with best-fit lines overlying data points. Slope s_o is the mean value of the ratio of signal amplitudes between two interferograms, found using a nonbiased linear regression. Slopes s_{xy} and s_{yx} provide uncertainty bounds for the slope estimates. Both are calculated using a standard least-squares technique in which s_{xy} is the best-fit line when the dependent variable holds all the variance and s_{yx} is the best-fit line when the independent variable holds all the variance.

Table 1
Inteferogram Ratios Acquired from Four Postseismic Pairs, with Corresponding Slopes and Sigma Values

Ratio	t_{ref}	t_{rep}	t^{ref}	t^{rep}	s_o	s_{xy}	s_{yx}	σ
R_1^4	4	249	39	354	0.686	0.642	0.733	.0450
R_1^3	4	249	74	319	0.821	0.725	0.929	.1010
R_1^2	4	249	39	144	0.509	0.477	0.544	.0330
R_3^2	74	319	39	144	0.620	0.574	0.671	.0710
R_4^2	39	354	39	144	0.742	0.707	0.780	.0360
R_4^3	39	354	74	319	1.20	1.05	1.36	.1550

t is in days after the 16 October 1999 Hector Mine earthquake.
Subscripts ref and rep refer to ratio subscript interferogram number.
Superscripts ref and rep refer to ratio superscript interferogram number.

two candidate mechanisms (e.g., Pollitz *et al.*, 2001). Unfortunately, on spatial scales in excess of a few tens of kilometers (i.e., corresponding to the deformation processes in the lower crust) the observed postseismic LOS displacements are small (1–2 cm) and uncorrelated between independent interferograms, making them difficult to interpret in terms of tectonic deformation. Indeed, we performed the above regression analysis on the interferogram pairs using the full 100 km $\times$ 100 km displacement map (Fig. 1). The data are highly scattered and show no common features among the

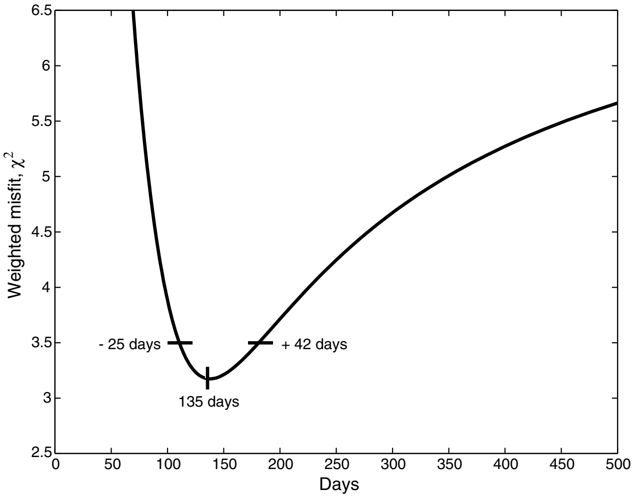

Figure 7. Plot of estimated relaxation time for the Hector Mine earthquake. Our calculated relaxation time is 135 $+42$ or -25 days. The uncertainty bounds are taken at the points where the χ^2 curve is 10% greater than the minimum.

interferograms on the larger scale. Conversely, the near-fault LOS anomalies are quite persistent in different interferograms, most likely indicating shallow deformation on or near the earthquake rupture. Here we investigate the possibility that the postseismic LOS displacements near the Hector Mine rupture result from shallow afterslip or volume changes (or both) on the earthquake fault.

Postseismic Deformation Model

The LOS displacements from only one satellite look direction do not allow one to distinguish between the horizontal and vertical components of deformation (e.g., Fialko *et al.*, 2001). In our analysis therefore, we use data from both the descending and ascending orbits that span a similar time interval, from about 1 month to about 1 year after the earthquake. The corresponding interferograms are shown in Figures 8a and 8b. The raw InSAR data were processed using the JPL/Caltech software package ROI_PAC, and a mosaic of 7.5-min USGS digital elevation maps with 30-m postings. Unfortunately, no independent interferometric postseismic pairs are available from the ascending orbit, so we cannot verify what part of a signal shown in Figure 8b might be due to atmospheric effects; however, both the LOS increase near the releasing fault bend to the north-west of the epicenter and the LOS decrease around the epicenter common to all four descending interferograms are also apparent in the ascending interferogram, suggesting that these LOS displacements represent mostly vertical motion. The area immediately to the southwest of the epicenter is more complicated, as it is characterized by LOS decrease in the descending interferogram and LOS increase in the ascending interferogram.

We model the postseismic signal revealed by the InSAR data using the fault geometry that best explains the coseismic displacement field (Simons *et al.*, 2002). The fault is represented by four rectangular segments that are subdivided into individual slip patches whose size is chosen to yield a uniform model resolution. The position of the top edges of the fault segments are denoted by magenta lines in Figure 8. The fault subpatches are approximated by finite dislocations in an elastic half-space (e.g., Okada, 1985). Our goal is to find a slip distribution on the model fault that best explains the observed postseismic LOS data. The best-fitting slip distribution is found through a constrained least-square minimization (for details of the inversion technique, see Simons *et al.*, 2002). We perform a number of simulations in which we vary both the number of degrees of freedom for slip on the individual fault segments and the degree of smoothing. Initially, a linear inversion is done, for the overall sense of pure strike slip on the fault segments, in which we impose no constraints on the slip direction but use relatively heavy smoothing to prevent spurious checkerboarding slip patterns. These simulations indicate that the data are most consistent with the right-lateral sense of slip on the earthquake rupture. In the subsequent simulations, we restrict strike slip to be right-lateral and reduce the degree of smoothing until some compromise is found between the quality of fit to the data and the model roughness. We find that neither the pure strike slip, nor a combination of strike and dip slip, on the Hector Mine rupture produces the near-fault subsidence and uplift patterns seen in Figures 8a and 8b. Allowing for the fault-normal displacement component results in a qualitatively better fit to the data. Next, we impose a sign constraint on the fault-normal displacements using the same approach as described above for the strike slip mode. From this constraint, the fault-normal contraction is found to be the dominant mode for volume changes on the fault plane and seems to be required by the data. The reduction in the RMS misfit between the data and the model predictions is 33%, 42%, and 52% for the pure strike slip; strike and dip slip; and a combination of the strike-slip, dip-slip, and fault-normal contraction, respectively. Figures 8c and 8d show predictions of our preferred model, which includes the spatially varying strike-slip, dip-slip, and fault-normal displacements, and Figure 8e shows the inferred distribution of slip (arrows) and fault-normal contraction (color).

The best-fitting model (Figure 8e) shows up to a few tens of centimeters of predominantly strike-slip (right-lateral) subsurface motion along the uppermost several kilometers of the fault, especially on the north-northwest-trending splay that did not break the surface during the earthquake (segment 3 in Fig. 8), and up to ten centimeters of fault-normal contraction near the fault bends. The magnitude of afterslip seems to anticorrelate with the coseismic slip magnitude (see Simons *et al.*, [2002, their Fig. 9]). In particular, segment 2, which had the largest coseismic displacement, is characterized by the smallest afterslip. We point out that fault contraction is required to explain the

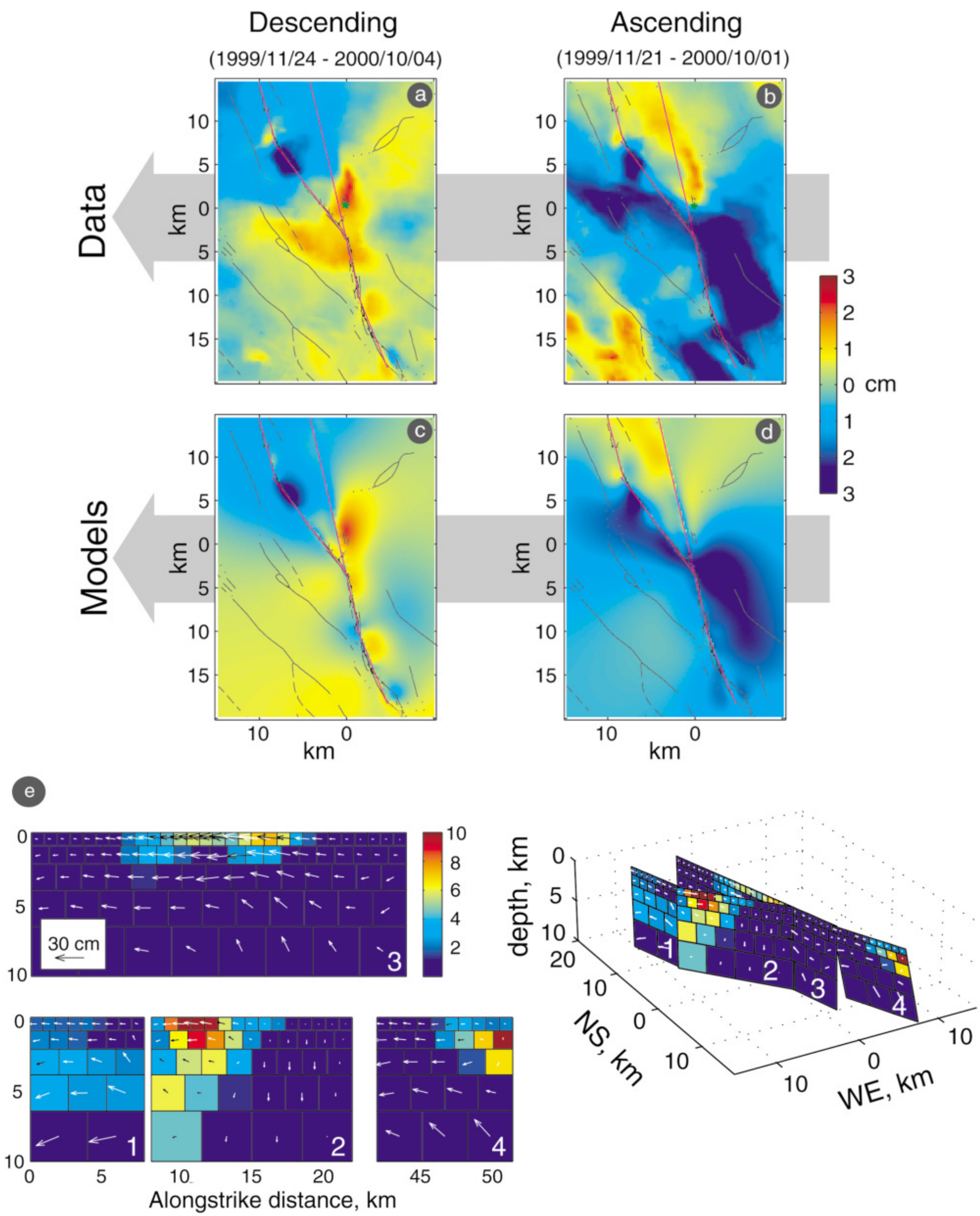

Figure 8. (a) Descending and (b) ascending postseismic LOS displacements (positive toward the radar); (c) and (d), predictions of our preferred model, which includes the spatially varying strike-slip, dip-slip, and fault-normal displacements; (e) best-fitting model, with arrows denoting the inferred slip distribution and color denoting the fault-normal contraction.

subsidence area at the northern end of segment 2. Postseismic displacements on the fault are not well resolved at depths greater than about 5 km, because the LOS data at distances greater than several kilometers away from the fault are dominated by the atmospheric noise. The latter statement is corroborated by calculations assuming various depth of the fault afterslip. In particular, inversions in which the fault depth is taken to be 6 km give rise to an increase in the RMS misfit of only 2%, but inversions in which the fault depth is limited to 2 km increase the RMS misfit by more than 20%.

Integrating the strike slip over the fault area in the upper 5 km of the fault and using the typical shear modulus for the crust of 3.3×10^{11} Pa, we obtain an estimate for the postseismic moment release on the order of 10^{18} Nm. The deduced geodetic moment is at least an order of magnitude larger than the cumulative seismic moment of all aftershocks that occurred on or near the respective fault area (the aftershock catalog courtesy of E. Hauksson, [Hauksson *et al.*, 2002]). This suggests that most of the slip revealed by the InSAR data (Fig. 8) occurred aseismically.

The fault-normal contraction inferred from our analysis most likely indicates volume changes in the upper section of the Hector Mine rupture, although physical mechanisms responsible for such volume changes are not well understood. Peltzer *et al.* (1996, 1998) interpreted the InSAR observations of near-field deformation following the Landers rupture as indicating the hydraulic response of fluid-saturated rocks to coseismic changes in the ambient stress. Similarly, Massonnet *et al.* (1996) suggested that postseismic deformation along some sections of the rupture of the 1992 Landers earthquake indicated fault-zone collapse due to post-earthquake crack closure and fluid expulsion from the fluid-saturated fault core. Massonnet *et al.* (1996) interpreted the InSAR data from one look direction as indicating about 30 cm of fault closure in the depth interval between 6 and 11 km. Results shown in Figure 8 suggest that the fault-zone contraction following the Hector Mine earthquake is quite shallow (the uppermost 3 to 4 km) and likely extends to the surface. To the best of our knowledge, no surface manifestations of fluid expulsion from the fault zone have been observed. An alternative explanation is that the fault zone contraction may be caused by the porosity reduction (which may or may not involve fluid flow). The latter interpretation implies that a comparable increase in porosity is created coseismically due to the enhanced dilatancy in the releasing bends of a strike-slip fault. The systematic centimeter-scale misfit between the coseismic interferograms and the slip model that assumes no fault-normal displacements (Simons *et al.*, 2002) may be consistent with the local dilatancy effects, although the signal is too small compared to the coseismic LOS displacements to allow a robust interpretation.

Conclusion

Postseismic displacement maps derived from ERS SAR data provide significant information on the structural deformation in the area of the Lavic Lake fault rupture. Large zones of subsidence and uplift occur near the northern end of the rupture, and a narrow trough runs along the fault. We interpret the region of uplift and the trough as characteristics of a right-lateral, strike-slip fault with a double left-bend. The cause of the northwestern zone of subsidence remains unclear. Subsequent interferograms continue to exhibit these structural signatures, but to a lesser magnitude. All interferograms display a high–low signal at the northern end of the rupture. We isolate this pattern and use a nonbiased linear regression to constrain a near-field relaxation of $135\ +42$ or -25 days. Since our relaxation time compares well to the Landers earthquake decay rate estimated by Savage and Svarc (1997) of 84 ± 23 days, we infer that the acting near-field postseismic relaxation processes are similar. Using an interferogram along an ascending orbit to obtain a second component of surface deformation, we confirm that most of the near-field postseismic deformation is vertical. Moreover, we develop an afterslip model that is consistent with both the ascending and descending interferograms. A necessary feature of the model is a component of fault-zone collapse. Future data acquisitions by the ERS-2 satellite along ascending orbits will provide better constraints on the vector postseismic displacements.

Acknowledgments

SAR data were provided by the European Space Agency through its distributors SpotImage and Eurimage. Data were purchased by the WInSAR consortium with funding from NASA, USGS, and NSF. The research was funded by the Southern California Earthquake Center and the National Science Foundation (EAR-0105896 and EAR-9977823).

References

Agnew, D. C., S. Owen, Z. K. Shen, G. Anderson, J. Svarc, H. Johnson, K. E. Austin, and R. Reilinger (2002). Coseismic displacements from the Hector Mine, California, earthquake: results from survey-mode GPS measurements, *Bull. Seism. Soc. Am.* **92,** 1355–1364 (this issue).

Bock, Y., S. Wdowinski, P. Fang, J. Zhang, S. Williams, H. Johnson, J. Behr, J. Genrich, J. Dean, M. van Domselaar, D. C. Agnew, F. K. Wyatt, K. Stark, B. Oral, K. W. Hudnut, R. W. King, T. A. Herring, S. J. Dinardo, W. Yound, D. D. Jackson, and W. Gurtner (1997). Southern California permanent GPS geodetic array: continuous measurements of regional crustal deformation between the 1992 Landers and 1994 Northridge earthquakes, *J. Geophys. Res.* **102,** (B8), 18,013–19,033.

Crowell, J. C. (1974). Origin of Late Cenozoic Basins in Southern California, Soc. Econ. Paleontologists and Mineralogists, Special Publication No. 22, 190–204.

Davis, G. H., and S. J. Reynolds (1996). *Structural Geology of Rocks and Regions* John Wiley and Sons, New York, 366–371.

Deng, J., M. Gurnis, H. Kanamori, and E. Hauksson (1998). Viscoelastic flow in the lower crust after the 1992 Landers, California, earthquake, *Science* **282,** 1689–1692.

Dibblee, T. W., Jr. (1966). Geologic map of the Lavic quadrangle, San Bernardino County, California: U.S. Geol. Survey, Misc. Geol. Investigations map, I-472, scale 1:62,500.

Dokka, R. K., and C. J. Travis (1990). Role of eastern California shear zone in accommodating Pacific–North America plate motion, *Geophys. Res. Lett.* **17,** No. 9, 1323–1326.

Fialko, Y., M. Simmons, and D. C. Agnew (2001). The complete (3-D) surface displacement field in the epicentral area of the 1999 M_w 7.1 Hector Mine earthquake, California, from space geodetic observations, *Geophys. Res. Lett.* **28,** no. 16, 3063–3066.

Goldstein, R. M., H. A. Zebker, and C. L. Werner (1988). Satellite radar interferometry two-dimensional phase unwrapping, *Radio Sci.* **23,** 713–720.

Hauksson, E., L. M. Jones, and K. Hutton (2002). The 1999 M_w 7.1 Hector Mine, California, earthquake sequence: complex conjugate strike-slip faulting, *Bull. Seism. Soc. Am.* **92,** 1154–1170 (this issue).

Hurst, K. J., D. F. Argus, A. Donnellan, M. B. Heflin, D. C. Jefferson, G. A. Lyzenga, J. W. Parker, M. Smith, F. H. Webb, and J. H. Zumberge (2000). The coseismic geodetic signature of the 1999 Hector Mine Earthquake, *Geophys. Res. Lett.* **27,** no. 17, 2733–2736.

Kermack, K. A., and J. B. S. Haldane (1950). Organic correlation and allometry, *Biometrika* **37,** 30–41.

Mark, D. M., and M. Church (1977). On the misuse of regression in earth science, *Math. Geol.* **9,** 63–75.

Massonnet, D., and K. L. Feigl (1998). Radar interferometry and its application to changes in the Earth's surface, *Rev. Geophys.* **36,** no. 4, 441–500.

Massonnet, D., K. Feigl, M. Rossi, and F. Adragna (1994). Radar interferometric mapping of deformation in the year after the Landers earthquake, *Nature* **369,** 227–230.

Massonnet, D., M. Rossi, C. Carmona, F. Adragna, G. Peltzer, K. Fiegl, and T. Rabaute (1993). The displacement field of the Landers earthquake mapped by radar interferometry, *Nature* **364,** 138–142.

Massonnet, D., W. Thatcher, and H. Vadon (1996). Detection of postseismic fault-zone collapse following the Landers earthquake, *Nature* **382,** 612–616.

Okada, Y. (1985). Surface deformation to shear and tensile faults in a half-space, *Bull. Seism. Soc. Am.* **75,** 1135–1154.

Owen, S., G. Anderson, D. C. Agnew, H. Johnson, K. Hurst, R. Reiinger, Z.-K. Shen, J. Svarc, and T. Baker (2002). Early postseismic deformation from the 16 October 1999 M_w 7.1 Hector Mine, California, earthquake as measured by survey-mode GPS, *Bull. Seism. Soc. Am.* **92,** 1423–1432 (this issue).

Peltzer, G., P. Rosen, F. Rogez, and K. Hudnut (1996). Postseismic rebound in fault step-overs caused by pore fluid flow, *Science* **273,** 1202–1204.

Peltzer, G., P. Rosen, F. Rogez, and K. Hudnut (1998). Poro-elastic rebound along the Landers 1992 earthquake surface rupture, *J. Geophys. Res* **103,** 30,131–30,145.

Pollitz, F., C. Wicks, and W. Thatcher (2001). Mantle flow beneath a continental strike-slip fault: postseismic deformation after the 1999 Hector Mine earthquake, *Science* **293,** 1814–1818.

Price, E. J. (1999). Coseismic and postseismic deformation associated with the 1992 Landers, California, earthquake measured by synthetic aperture radar, *Ph.D. Thesis*, Scripps Institution of Oceanography, La Jolla, California, 1–19, 123–157.

Rosen, P. A., S. Hensley, I. R. Joughin, F. K. Li, S. N. Madsen, E. Rodriguez, and R. M. Goldstein (2000). Synthetic aperture radar interferometry, *Proc. IEEE* **80,** no. 3, 333–382.

Sandwell, D. T., L. Sichoix, and B. Smith (2002). Hector Mine earthquake: vector near-field displacements from ERS InSAR, *Bull. Seism. Soc. Am.* **92,** 1341–1354 (this issue).

Savage, J. C., and J. L. Svarc (1997). Postseismic deformation associated with the 1992 $M_w = 7.3$ Landers earthquake, southern California, *J. Geophys. Res.* **102,** 7565–7577.

Scharroo, R., and P. Visser (1998). Precise orbit determination and gravity field improvement for the ERS satellites, *J. Geophys. Res.* **103,** 8113–8127.

Scientists of the U.S. Geological Survey, the Southern California Earthquake Center, and the California Division of Mines and Geology (2000). Preliminary Report on the 16 October 1999 *M* 7.1 Hector Mine, California, earthquake, *Seism. Res. Lett.* **71,** 11–23.

Shen, Z.-K. D. D. Jackson, Y. Feng, M. Cline, M. Kim, P. Fang, and Y. Bock (1994). Postseismic deformation following the Landers earthquake, California, 28 June 1992, *Bull. Seism. Soc. Am.* **84,** 780–791.

Simons, M., Y. Fialko, and L. Rivera (2002) Coseismic static deformation due to the 1999 M_w 7.1 Hector Mine earthquake, California, as inferred from InSAR and GPS observations, *Bull. Seism. Soc. Am.* **92,** 1390–1402 (this issue).

Treiman, J. A., K. J. Kendrick, W. A. Bryant, T. K. Rockwell, and S. F. McGill (2002) Primary surface rupture associated with the M_w 7.1 16 October 1999 Hector Mine earthquake, San Bernardino County, California, *Bull. Seism. Soc. Am.* **92,** 1171–1191 (this issue).

Zebker, H. A., P. A. Rosen, R. M. Goldstein, A. Gabriel, and C. L. Werner (1994). On the derivation of coseismic displacement fields using differential radar interferometry: the Landers earthquake, *J. Geophys. Res.* **99,** 19,617–19,634.

Institute of Geophysics and Planetary Physics
Scripps Institution of Oceanography
University of California, San Diego
La Jolla, California 92093-0225

Manuscript received 18 October 2000.